Delft University of Technology

Evaluation of solidification cracking susceptibility during laser welding in advanced high strength automotive steels

Agarwal, G.; Kumar, A.; Richardson, I. M.; Hermans, M. J.M.

Important note
To cite this publication, please use the final published version (if applicable).
Please check the document version above.

Evaluation of solidification cracking susceptibility during laser welding in advanced high strength automotive steels

G. Agarwal*, A. Kumar, I.M. Richardson, M.J.M. Hermans

Department of Materials Science and Engineering, Faculty of 3mE, Delft University of Technology, Mekelweg 2, 2628CD Delft, the Netherlands

HIGHLIGHTS

- Weld solidification cracking is studied in two advanced high strength TRIP (high phosphorus) and DP (low phosphorus) steel sheets.
- Metallurgical factors for cracking includes morphology of the solidifying grains, interface growth rate and segregation of phosphorus.
- Thermal diffusivity is an important consideration that affects the weld pool shape and also the cracking behaviour.
- A sufficiently accurate thermal model can predict the weld pool shape and allows to achieve favourable conditions to avoid cracking.

GRAPHICAL ABSTRACT
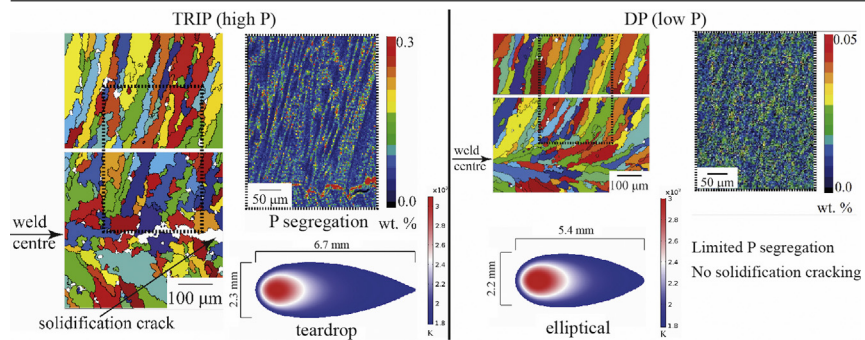
ABSTRACT

Solidification cracking susceptibility during laser welding was studied experimentally and numerically in advanced high strength steel sheets, namely transformation-induced plasticity (TRIP) and dual phase (DP) steel. Using the same heat input, laser bead-on-plate welding was carried out on single sided clamped specimens at various starting distances from the free edge. It was observed that TRIP steel with high phosphorus is susceptible to cracking while in DP steel with low phosphorus, solidification cracking was not observed. The metallurgical factors affecting the solidification cracking were studied and it was found that solidification morphology, phosphorus segregation at the prior austenite grain boundaries, inclusions, interface growth rate and interdendritic liquid feeding have a prominent effect on the strength of the mushy zone. These results are discussed pertaining to the cracking mechanism. For the same welding parameters, a difference in the weld pool shape was observed in both the steels, which is attributed to the high temperature thermophysical properties. Weld pool shape affects the strain distribution in the mushy region and thus the cracking behaviour. The cracking phenomenon is further described using hot ductility curves.

1. Introduction

Solidification cracking is a highly complex phenomenon in welding [1, 2], which is similar to hot tearing in casting [3, 4]. Solidification cracks are distinguished from other forms of cracks such as cold cracks and ductility dip cracks [5, 6], in that these occur above the solidus temperature. Solidification cracks initiate in the mushy zone as a result of thermal stresses/strains that are generated due to solidification shrinkage and thermal contraction. The stresses/strain are transmitted when there is an appreciable degree of coherency in the mushy zone. The liquid phase is still present in the form of films separating the grain boundaries [4]. At this stage, the solid fraction is typically greater than 0.94 [7]; any opening at the grain boundary

is difficult to fill with the remaining liquid due to low permeability. Usually, the condition is further aggravated by the presence of under-cooled liquid (extended solidification temperature range) due to the solute enrichment in the liquid, ahead of the solid-liquid interface [8]. If sufficient thermal strains are present, cracking occurs at the grain boundaries where liquid films act as a brittle phase. In this respect, hot tearing refers to the tearing up of the liquid film(s).

The CO_2 emission regulation of passenger vehicles has become stringent in the last two decades and the target emission between 2020–2025 converge globally [9]. One of the fundamental ways to achieve this target in the automotive industry is to reduce the over-all weight of the vehicle. Naturally, reduction of weight should not compromise the vehicle performance and passenger safety. To meet this demand, new steels under the umbrella of AHSS (Advanced High Strength Steel) are being increasingly developed and adopted. These steels account on an average for 30–35% of a typical car body weight [10] and possess high strength, ductility and toughness. The increased strength and ductility allows the use of thinner gauge steels, thus reducing the vehicle weight.[1] The AHSSs used in the automotive industry normally include dual-phase (DP) steel, transformation-induced plasticity (TRIP) steel, twinning-induced plasticity (TWIP) steel, complex phase (CP) steel and martensitic steel with tensile strength and ductility varying from 600 to 1200 MPa and 40–10 % respectively [11, 12]. Typically, these steels are used as chassis components, B-pillars, crash boxes, engine cradles *etc.* [12].

Apart from formability requirements in these steels, weldability of such steels is important. The higher content of alloying elements in some of the AHSSs, required for achieving necessary mechanical properties render them susceptible to solidification cracking during welding. Some automotive manufacturers have reported solidification cracking in assembling parts during laser welding. For instance, Larsson reported solidification cracking during laser welding of the B-pillar used in the Volvo XC60 [13]. Typically, pre-formed parts are welded in a flange geometry and the width of the flange can be reduced compared to flange width required for resistance spot welding to decrease the weight of the car body. When welding is carried out below a critical distance from the edge, solidification cracking may occur. This can lead to process instabilities and part rejection. Ideally, the solidification cracking sensitivity should be considered at the design stage of new alloys. Additionally, processing techniques such as additive manufacturing and casting involving fusion of materials also require understanding of solidification cracking phenomenon.

Two fundamental factors generated by the weld thermal cycle are responsible for solidification cracking; firstly the restraint, which is usually the mechanical or thermal stresses/strains and secondly, the solidifying microstructure. Metallurgical factors that affect the crack-ing susceptibility include solidification temperature range, solute segregation, surface tension and viscosity of the interdendritic liquid, liquid feeding tendency, grain morphology and dendritic coherency. It is the complex interaction of restraint and solidifying microstruc-ture that leads to solidification cracking. Fig. 1 outlines the various aspects that affect these two fundamental factors [1, 14].

In the past, efforts have been made to understand the underly-ing mechanisms responsible for solidification cracking [15-17]. The existing theories on solidification cracking behaviour include critical stress based, strain based and strain rate based criteria [18]. The early work of Feurer [19] was based on rate of feeding and rate of shrinkage effects on hot cracking phenomena. Cracking occurs if during solidi-fication, the volume rate of feeding of the liquid in the inter-dendritic region is less than the volume rate of shrinkage of the solid being formed. However, thermal strains in the solid in the mushy zone were not considered in his work. Significant advances were made

by Rappaz, Drezet and Gremaud [20]. The RDG model also includes thermal contraction as well as interdendritic fluid flow. A constant critical strain rate was proposed beyond which cavitation/cracking occurs. Localisation of the strain rate in the mushy zone was not con-sidered. In contradiction to the RDG model, Coniglio and Cross [21] asserted that pore nucleation by liquid fracture is unlikely to occur and proposed a porosity-based crack initiation model. Instead of con-sidering the whole mushy region, a recent model by Kou [22] focuses on the grain boundaries and the associated solidification shrinkage, thermal deformation and liquid feeding. An index for susceptibility to cracking was proposed based on the steepness of the $T - \sqrt{f_s}$ curve, near $\sqrt{f_s} = 1$, where T is the temperature and f_s is the fraction of solid. The steeper this curve, the higher the cracking susceptibility. Both the RDG and Kou models are sensitive to the actual solidifi-cation curves ($T - f_s$) particularly for high solid fraction values. It is important to note that all the existing models provide an indica-tion of susceptibility to solidification cracking. For actual cracking behaviour the conditions shown in Fig. 1 should be considered.

In this manuscript, solidification cracking phenomena is studied in two commercial AHSS, namely TRIP and DP steels sheets. These steels are widely employed in automotive car bodies [11] and hence make a good case for the present study. The extent of the contributing factors that lead to solidification cracking is discussed, with emphasis on the role of the weld pool shape and solidification morphology. It is shown that the weld pool shape, specifically at the tail region, is affected by the temperature dependent thermophysical properties of a material.

2. Methodology

2.1. Welding arrangement

Commercial TRIP and DP steel sheets of thickness 1.25 mm were selected. The compositions of the steels are listed in Table 1. The equilibrium solidification temperature range of TRIP and DP steel was obtained using the commercial software Thermo-Calc™ and was found to be 50 K and 33 K, respectively [23]. The hot cracking test used in the present work is based on the VDEh standard hot cracking test [24]. Bead-on-plate laser welding experiments were conducted parallel to the free edge at various starting positions with respect to the free edge, as described in reference [25]. To vary the amount of restraint, the starting distance of welding from the free edge was increased. The scheme of the experiments is listed in Table 2. In all the experiments, the nominal heat input was 110 J mm^{-1} while changing simultaneously the laser power and travel speed (cases A to E). With this heat input a fully penetrated weld was obtained in all the cases. Each experiment was repeated five times using a 3 kW Nd:YAG laser (Trumpf HAAS HL3006D). Specimens were kept at the focal point of the optical system with the laser spot size being 0.45 mm. In the assembly lines of car manufacturers, laser welding is generally carried out without the use of shielding gas. Also, the hot cracking test standard does not mention the use of shielding gas. To assess the effect of shielding gas on solidification cracking susceptibility, initial welding experiments were performed both with and without shielding gas. No difference in cracking tendency was observed and further tests were therefore carried out without a shielding gas to more closely mimic the industrial procedure. An optical high speed camera was used to capture the images during welding. The region of interest was on the specimen surface behind the laser spot and images were captured at a rate of 500 frames per second. The camera was positioned sideways with respect to the specimen.

2.2. Microstructural characterization

The weld surface was prepared for optical microscopy using standard metallographic procedure. Etching was carried out using

---

[1] Emission from primary steel production is 7–8 times less compared to its alter-native, aluminium [10]. Therefore, for overall reduction in emissions and production cost, steels are still the preferred choice in the automotive industry.
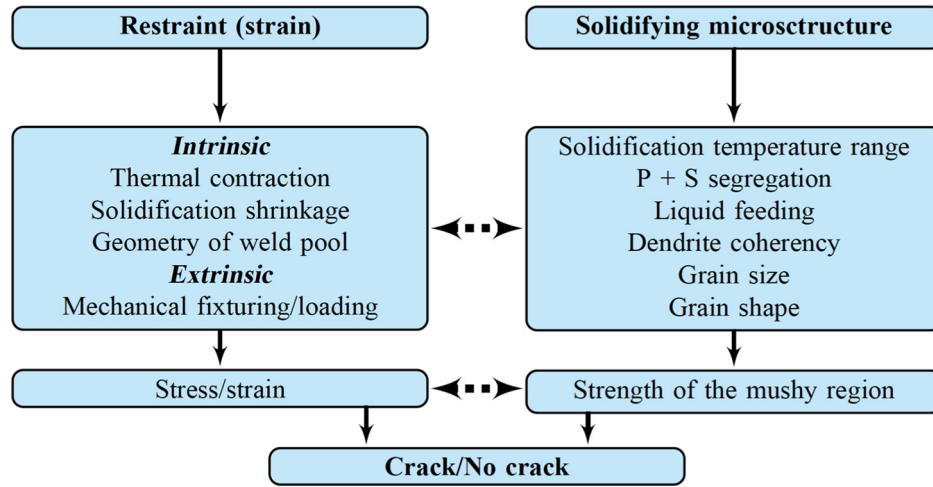
Fig. 1. Fundamental factors affecting solidification cracking.

4% Picral and 2% aqueous sodium metabisulfite. Scanning electron microscopy (SEM) was performed on the weld topside and fracture surface using a JEOL JSM 6500F™ microscope. Energy Dispersive Spectroscopy (EDS) analysis, in conjunction with SEM, was conducted on the weld topside to qualitatively examine the inclusions. Wavelength Dispersive Spectroscopy (WDS) was performed for mapping of elements on the weld surface using a JEOL JXA 8900R™ electron probe micro analyser (EPMA). Electron beam energy 15 kV and probe current 50 nA was used.

Due to post welding cooling rates in excess of 10^2 K s^{-1} [26, 27], the microstructure of the weld metal is predominantly martensitic. In order to determine the microstructural features of the weld, such as solidification substructure and grain orientation, knowledge of the parent grains, i.e. austenite is needed. Cayron et al. [28] proposed a method for reconstruction of the austenite grains in steels based on the ferrite orientations of lath martensite. The austenite grain structure is reconstructed by assuming that the orientation relationship (OR) between the lath martensite and the parent austenite is either Kurdjumov-Sachs (K-S) or Nishiyama-Wassermann (N-W). For this purpose, use of a computer program ARPGE developed by Cayron [29] was used. The weld surface was prepared for electron backscatter diffraction (EBSD) measurements by mechanical polishing using colloidal silica. EBSD at an accelerating voltage of 15 kV was performed to obtain ferrite orientation maps with a step size of 1 μm following the procedure in Ref. [30]. A minimum confidence index (CI) of 0.1 was used for parent grain reconstruction.

Table 1
Composition of the TRIP and DP steels used in this work (in weight %).

Elements, wt%	C	Mn	Al	Si	Cr	P	S
TRIP	0.19	1.63	1.1	0.35	0.019	0.089	0.005
DP	0.15	2.3	0.03	0.10	0.56	0.01	≈ 0

Table 2
Experimental scheme.

Cases	Distance from the free edge (mm)	Welding parameters	
		Laser power (W)	Speed (mm s^{-1})
A		1100	10
B	5	990	9
C		880	8
D		770	7
E	7	1100	10

2.3. Finite element modeling

In this work, a 3D finite element (FE) thermal model was utilised for laser bead-on-plate welding. A frequently used [31-33] 3D conical Gaussian heat source was adopted to describe the laser beam heat input. More details on the model are available in the reference [25].

The thermal history, i.e, temperatures (T) at (x, y, z, t) was obtained by solving the following Fourier heat transfer equation using the temperature-dependent thermal properties of the material,

$$\frac{\partial}{\partial x}\left(k(T)\frac{\partial T}{\partial x}\right) + \frac{\partial}{\partial y}\left(k(T)\frac{\partial T}{\partial y}\right) + \frac{\partial}{\partial z}\left(k(T)\frac{\partial T}{\partial z}\right) + Q_v = \rho(T)C_p(T)\left(\frac{\partial T}{\partial t}\right).$$

$$(1)$$

Here, $k(T)$ is the temperature dependent thermal conductivity, $\rho(T)$ is the temperature dependent density, $C_p(T)$ is the temperature dependent specific heat capacity and Q_v is the net volumetric heat flux. The initial boundary condition for the transient analysis is given by

$$T(x, y, z, 0) = T_0,$$

$$(2)$$

where, T_0 is the ambient temperature taken as 293 K. The natural boundary condition, implicitly considered in the finite element analysis is,

$$k_n\frac{\partial T}{\partial n} - q + h(T - T_0) + \sigma\epsilon(T^4 - T_0^4) = 0.$$

$$(3)$$

The condition applies on the boundaries which are subjected to convection, radiation and heat flux. k_n is the thermal conductivity normal to the boundary, q is the imposed heat flux on the boundary due to the external heat source, h is the heat transfer coefficient for convection, σ is the Stefan-Boltzmann constant for radiation (5.67 × 10^{-8} W m^{-2} K^{-4}) and ϵ is the emissivity. The heat transfer coefficient was taken to be 10 W m^{-2} K^{-1} [34]. The emissivity was assumed to be a function of temperature (in K) based on the work of van der Aa [35], given by

$$\epsilon = 0.7 - 0.02\exp\left(\frac{900}{T}\right).$$

$$(4)$$

The thermophysical properties of the TRIP steel, *i.e.* density, thermal conductivity and specific heat capacity were taken from reference [36] and are shown in Fig. 2 (a–c). Note that the chemical composition of the TRIP steel used in Ref. [36] is similar to the TRIP steel used in this work. Moreover, it is reported in the reference that the properties were measured as a function of temperature up to 1723 K. At this temperature, the steel is still in the solid state. The latent heat data was taken from a commercial thermodynamic software, Thermo-Calc™ (database TCFE7). In the two phase region, the apparent heat capacity method was applied. The latent heat is included as an additional term in the heat capacity. The total heat capacity can be written as,

$$C_p = C_{p,solid}(1 - f_L(T)) + C_{p,liquid}f_L(T) + L\frac{df_L}{dT}, \tag{5}$$

where, $C_{p,solid}$ is the specific heat capacity of the solid, $C_{p,liquid}$ is the specific heat capacity of the liquid, f_L is the fraction of liquid and L is the latent heat of fusion. The apparent heat capacity was related to the temperature-phase fraction data, obtained using the Scheil-Gulliver solidification approximation. The apparent specific heat in the two phase region as a function of temperature is shown in Fig. 2 (d).

The thermophysical properties of DP steel used in the model are shown in Fig. 2(a–c). Thermal conductivity was measured as a function of temperature (room temperature, 473 K, 673 K, 873 K, 1073 K, 1273 K, 1473 K and 1623 K), using a laser flash apparatus (NETZSCH LFA 427), following the standard DIN EN 821/2 [37]. The thermal conductivity above 1623 K was assumed to be constant. Specific heat

was measured as a function of temperature, using differential scanning calorimetry (NETZSCH DSC 404 C), following the standard DIN EN 821/3 [38] until 1623 K. Density data was obtained using Thermo-Calc™ (database TCFE7). The apparent heat capacity for DP steel was calculated by the same procedure as described above and is shown in Fig. 2(d). The material properties at melting point (1787 K) were used for higher temperatures. Note that the effect of fluid flow on weld pool shape was not considered in the present work. An equivalent heat source (Gaussian type) was utilized without considering the effect of the keyhole. In order to study the effect of fluid flow comprehensively, keyhole should also be modeled as described in Refs. [39, 40].

The commercial finite element software, COMSOL™ (version 5.2) was used in the present work. Hexahedral elements (brick) were used for meshing the geometry. A minimum mesh size of $0.27 \times 0.417 \times 0.417$ mm^3 was used in the weld zone and gradually the mesh size was increased. The process efficiency of laser welding *i.e.*η was assumed to be 40% based on previous work of Pan [41] on a similar experimental arrangement. In this way, heat losses due to convection and radiation in the keyhole were taken into account.

3. Results and discussion

3.1. Observation of solidification cracking

In TRIP steel, solidification cracking was observed in all the cases except for case D (Table 2). In DP steel, solidification cracking was not observed in any of the cases. Fig. 3(a–b) show high-speed camera images taken during welding of TRIP steel for the cases A and E [23].
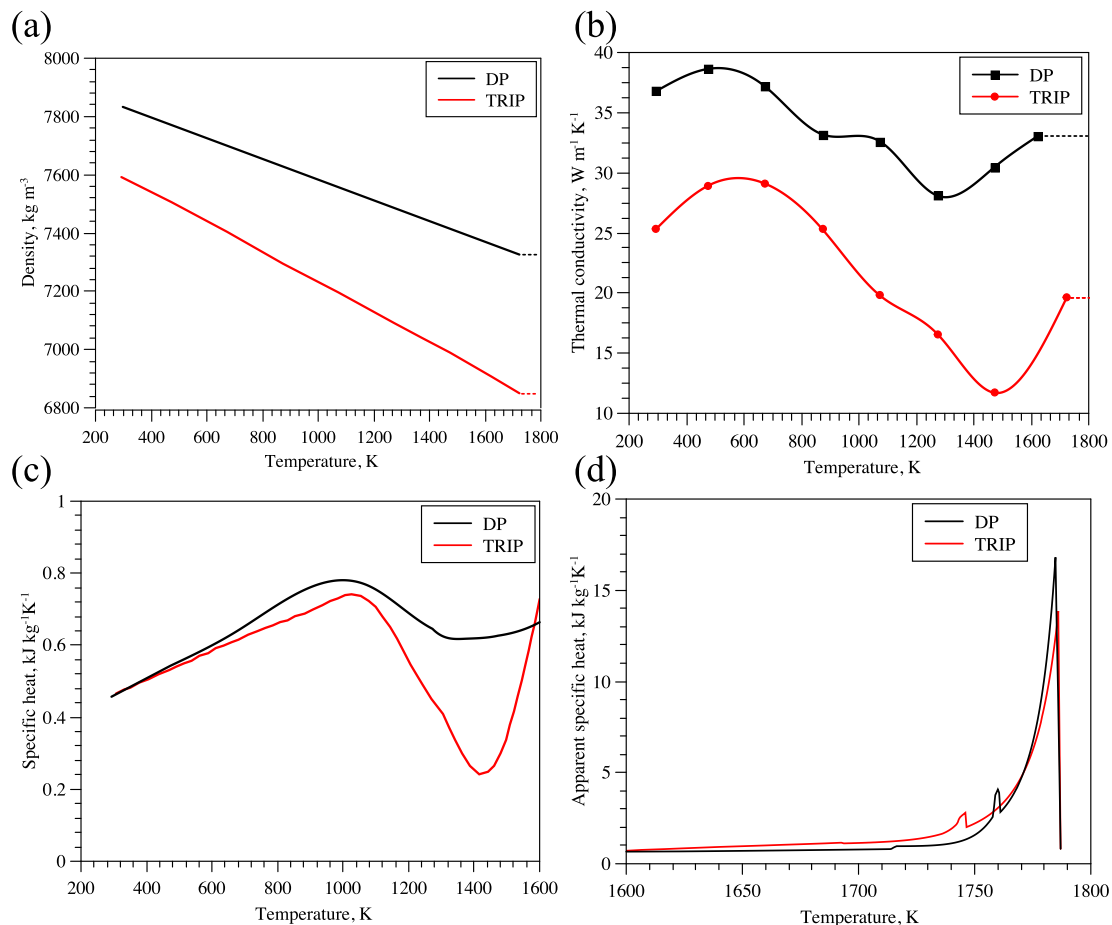

Fig. 2. Thermophysical properties of TRIP and DP steel. (a) Density as a function of temperature, (b) Thermal conductivity as a function of temperature, (c) specific heat as a function of temperature and (d) apparent specific heat as a function of temperature. Thermophysical properties of TRIP steel was taken from reference [36].
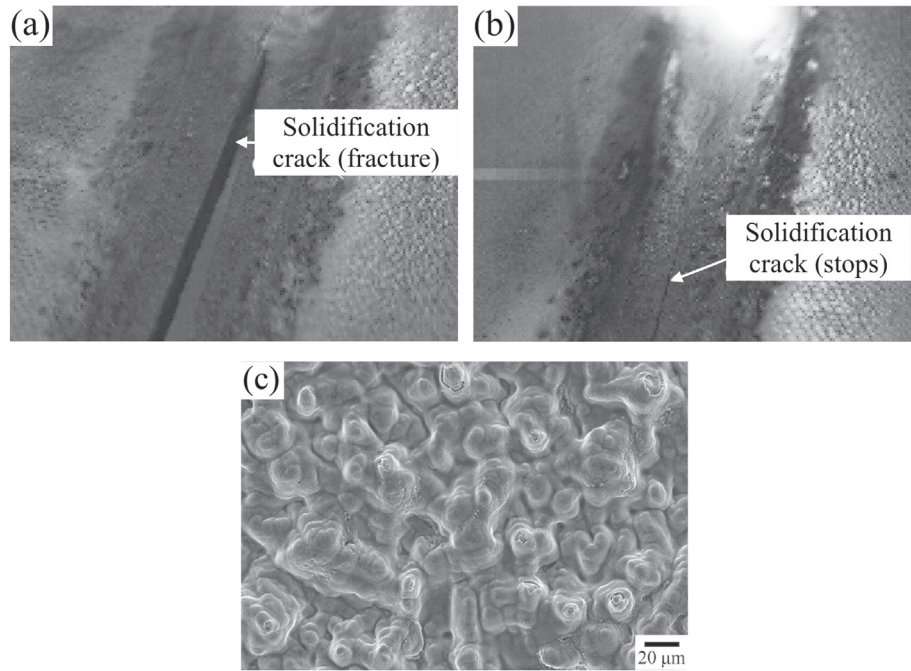
Fig. 3. High speed camera images during welding of TRIP steel for, (a) case A and (b) case E in Table 2, (c) secondary electron micrograph of the fracture surface showing dendritic morphology, a typical feature of solidification cracking.

A solidification crack at the weld centreline was observed to follow the heat source and complete fracture (Fig. 3(a)) occurred in cases A to C. Fig. 3(b) shows the image when welding was carried out at a distance of 7 mm from the free edge, *i.e.* case E. After a certain distance, the solidification crack ceased to propagate.

The fracture surface (Fig. 3(c)) shows a dendritic morphology indicating the presence of liquid film prior to the onset of solidification cracking. Such appearance of the fracture surface due to solidification cracking is common in various alloy systems [42, 43].

The susceptibility towards solidification cracking decreases, as the starting distance from the free edge increases. This observation is consistent with earlier studies [44, 45]. In our previous research, strains close to the fusion boundary were measured and calculated during welding [26]. The results showed that for the same welding parameters (laser power and speed), the transverse strain near the mushy zone decreases as the distance from the free edge increases [25, 46]. As the welding parameters remain the same, the weld pool shape and the solidifying microstructure does not change. Therefore, the cracking behaviour is entirely due to the restraint of the surrounding material.

3.2. Metallurgical factors affecting solidification cracking susceptibility

In this section, metallurgical factors which affect the solidification cracking behaviour in TRIP and DP steel, welded under the same conditions (case E in Table 2) are discussed. First, the weld pool shape and solidification morphology is discussed followed by the effects on the solid-liquid interface growth rate and solidification time. Furthermore, the effect of interdendritic liquid feeding is addressed. Finally, the effect of the strain distribution in the mushy zone on solidification cracking is elaborated.

3.2.1. Weld pool shape and solidification morphology
Fig. 4 (a, b) shows the macrographs of the weld surface TRIP and DP steel, respectively. The weld surfaces indicate that the grains continue to grow in one direction towards the centreline in TRIP steel, while in DP steel, grains bend continuously as they grow towards the

weld centreline. This observation was confirmed by the EBSD measurements (Fig. 4 (c, d)), showing the prior austenite grain color map. The Fig. 4(a–d) further indicate that in TRIP steel, the weld pool is teardrop shaped, while it is elliptical in DP steel.

The phosphorus elemental map in Fig. 4(e), obtained by EPMA, shows evidence of P segregation at the austenite grain boundaries in TRIP steel. The phosphorus elemental map in Fig. 4(f) for the DP steel, shows that P segregation is not that apparent in comparison with the TRIP steel. It should be noted that the DP steel has a low amount of P in the base metal (0.01 wt %) than the TRIP steel (0.89 wt %). In our previous work [47], notable segregation of phosphorus in TRIP steel was also found by atom probe tomography and phase field simulations.

The weld surface of the TRIP steel welds was probed for inclusions using scanning electron microscopy. Secondary electron micrographs and EDS analysis shown in Fig. 5 show aluminium-rich oxide, Fe_3P and AlN inclusions, which form during weld solidification [48, 49], particularly near the weld centreline. The melting point of Fe-Fe_3P eutectic is 1321 K[50], which confirms that the actual solidus temperature in some interdendritic regions of the weld falls 416K below the equilibrium solidus temperature (1737 K); significantly broadening the solidification temperature range. It should be noted that the inclusions of Al form at a significantly higher temperature than Fe_3P [48, 49] (Al_2O_3, AlN starts to form approximately at 2080 K and 1939 K[49], respectively) and contrary to Fe_3P, their presence is not an evidence of the presence of liquid metal below the equilibrium solidus temperature.

From elemental mapping and inclusion analysis in TRIP steel, it can be inferred that grain boundary liquid films in TRIP steel prevent the solidifying microstructure from forming a coherent network until a relatively low temperature is reached (<1321 K). In DP steel, inclusions were not found indicating a smaller solidification temperature range.

3.2.2. Influence of interface growth rate and solidification time
From the solidification morphology, as discussed in the previous section, the rate at which the solid-liquid interface propagates
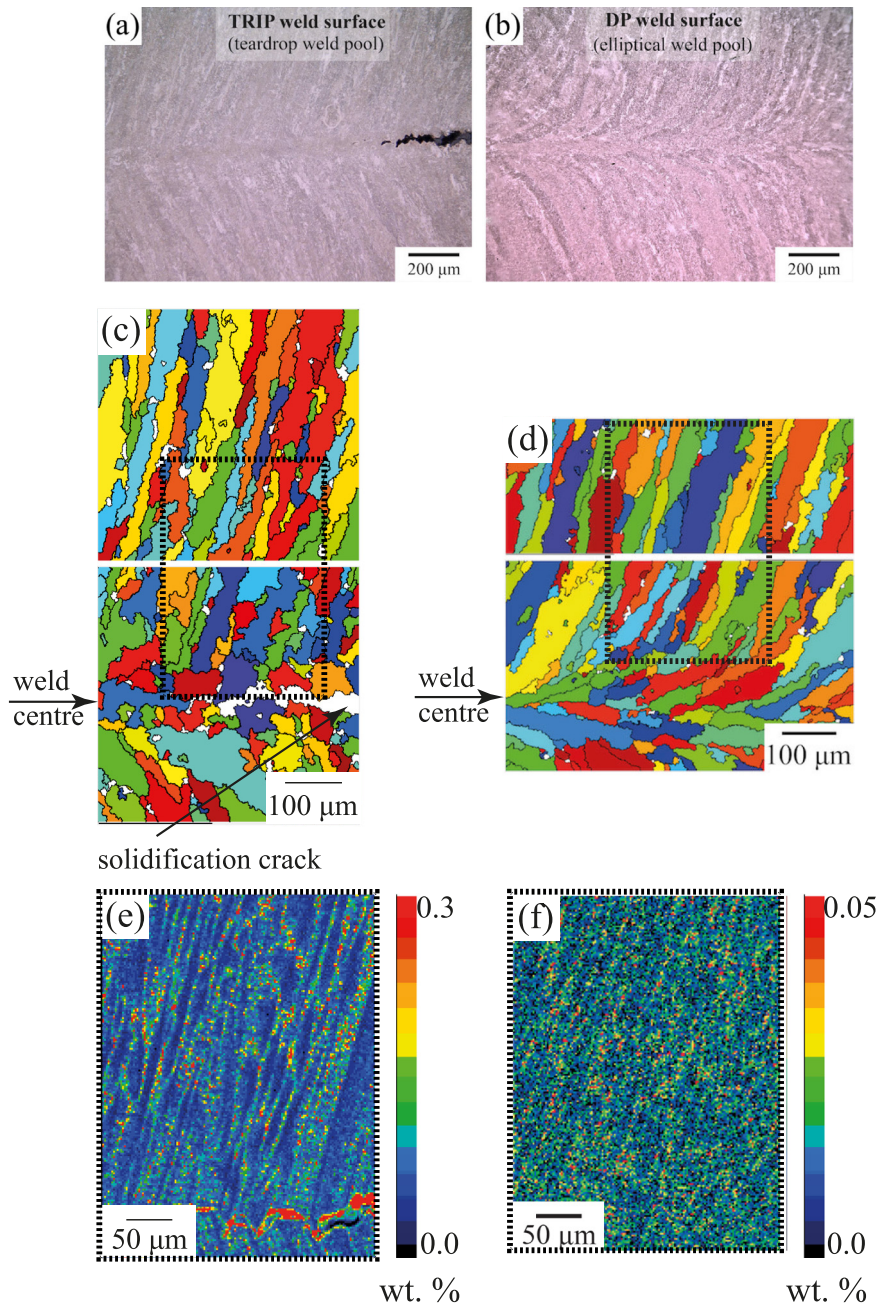
Fig. 4. Solidification morphology at the weld surface of TRIP and DP steels. (a, b) Optical micrographs, (c, d) prior austenite grains. (e, f) Phosphorus elemental maps in TRIP and DP steel welds. EPMA was performed within the regions indicated by the rectangular boxes in figures (c) and (d). The high phosphorus content in the crack in (e) is an instrumental artefact.

can be determined. During solidification, the interface grows in the direction of the maximum temperature gradient, *i.e.* normal to the interface. The interface growth rate is related to the heat source travel speed and is given by [51-53];

$$V_I = V_H \cos\theta \qquad (6)$$

where, V_H, V_I and θ are the heat source travel speed, interface growth rate and the included angle between the travel direction and interface normal. Due to the teardrop shape of the weld pool in TRIP steel, the direction of the maximum temperature gradient does not change much. However, in DP steel, due to the elliptical shape of

the weld pool, the direction of the maximum temperature gradient changes continuously. As a consequence, the interface growth rate also increases continuously in DP steel.

Based on the prior austenite grain color map of both the steels in the weld, macroscopic interface growth rate was calculated at various points from the weld centreline towards the fusion boundary (see Fig. 6). The term macroscopic is used because the preferential dendrite growth direction ⟨100⟩ is not considered in the present calculation. The interface growth rate was also calculated from the thermal model following the procedure in reference [54]. The calculated and experimental interface growth rate data are in reasonably good agreement. The results of the thermal model are further discussed in detail in Section 3.3.
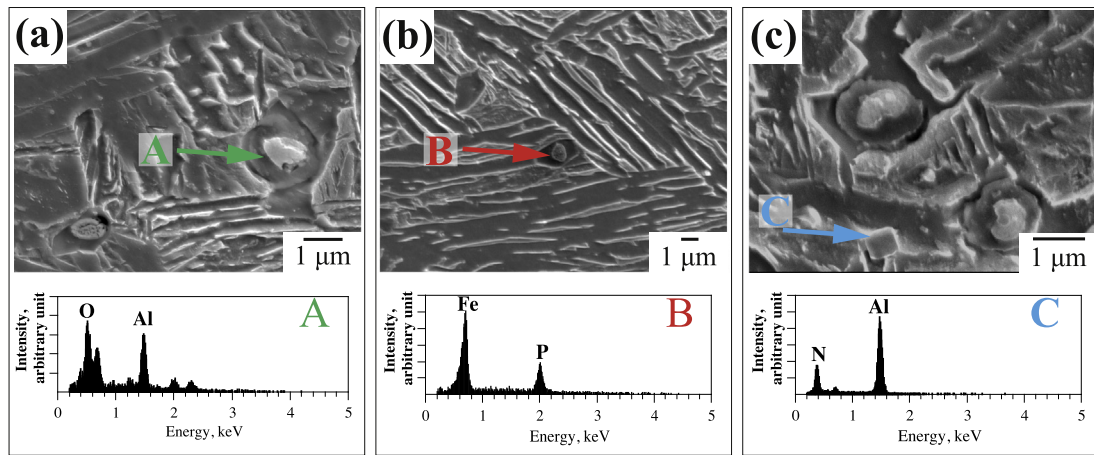
Fig. 5. Inclusions and EDS analyses on the weld surface of TRIP steel.

In TRIP steel, the interface growth rate is very slow near the fusion boundary and increases to a constant value near the centreline. In DP steel, the interface also propagates relatively slow at the fusion line but increases continuously, eventually growing with the same rate as that of the heat source near the centre. Therefore, the mushy region near the centre in TRIP steel spends considerably more time before solidification is completed. This allows segregation to take place on a larger scale and therefore the low melting point eutectic Fe-Fe$_3$P is observed near the centre (Fig. 5(b)).

In addition, the primary dendrite arm spacing (PDAS) and the secondary dendrite arm spacing (SDAS) are proportional to $(v^*)^{-1/4}G^{-1/2}$ and $(v^*G)^{-1/3}$, respectively [4]. Here, v^* is the dendrite tip velocity and G is the thermal gradient. Assuming the magnitude of the thermal gradient to be similar in both the steels and the dendrite tip velocity (v^*) to be proportional to the interface growth rate, both PDAS and SDAS should be larger in TRIP steel. Therefore, the coalescence temperature in the case of TRIP steel is reduced due to both higher interdendritic arm spacings and associated microsegregation.

As a result, the formation of a coherent solid network that can sustain transverse strain is delayed to low temperatures (or high solid fraction), increasing the cracking susceptibility.

To compliment the above analysis, a phase-field model of solidification was created, with focus on the solidification morphology in the tail of the weld pool. The details of the model are available in the reference [23]. Fig. 7 shows the solidification morphology (δ-ferrite) in TRIP steel and in DP steel with approximately the same solid fraction. The models also reveal that the secondary arm dendritic structure is more prominent in TRIP steel.

3.2.3. Interdendritic liquid feeding

Adequate liquid feeding in the interdendritic region is necessary to compensate for both the solidification shrinkage and thermal contraction of the solidifying dendrites, in order to avoid cracking. In our recent work [55], based on an *in situ* solidification study of these steels, liquid feeding in the interdendritic regions in DP steel was observed and cracks were not detected. However, in TRIP steel, cracking occurred during the last stages of solidification and liquid feeding was not encountered. Phase field simulation results revealed a large degree of undercooling and narrow liquid channels in TRIP
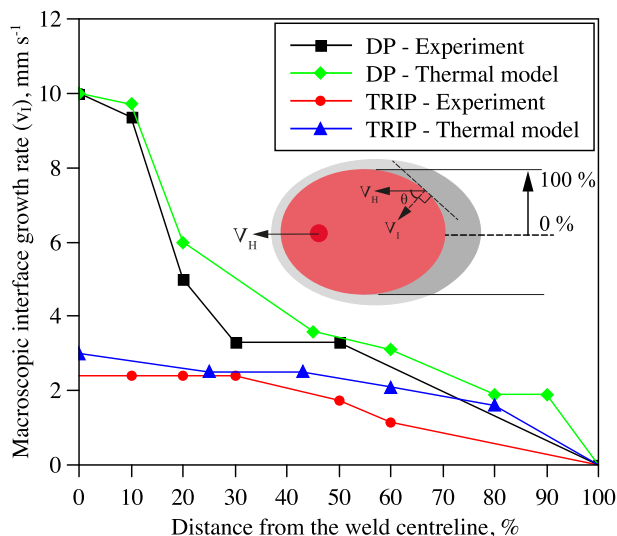

Fig. 6. Macroscopic interface growth rate as a function of distance from the weld centreline obtained both from the experiments (EBSD maps in Fig. 4) and the thermal model (presented later in Section 3.3). The inset schematic shows how the interface growth was determined at various points from the weld centreline on the EBSD maps.
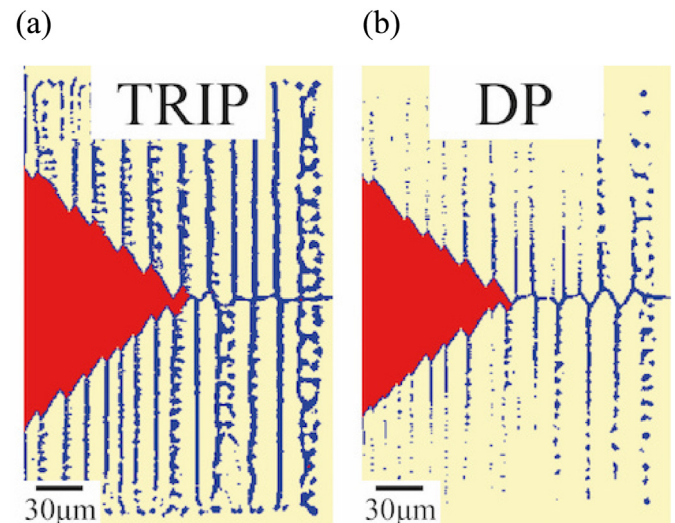

Fig. 7. Phase field simulation of solidification at the tail of the weld pool. (a) TRIP steel, (b) DP steel. Red color refers to the liquid, blue to the grain boundary and light yellow to the solid. (For interpretation of the references to color in this figure legend, the reader is referred to the web version of this article.)

steel, which act as a barrier for adequate liquid feeding [47]. Thus, insufficient liquid feeding is an additional factor that contributes to cracking in TRIP steel.

3.2.4. Strength of the mushy zone

The metallurgical factors discussed above determine the strength of the mushy zone, as also mentioned in Fig. 1. The stresses/strains described in Section 3.1 are imposed on the mushy region. An interplay between the induced stress and the strength of the mushy region dictates whether cracking occurs or not.

Fig. 8 shows the schematic representation of the effect of solidification morphology on solidification cracking. Owing to the difference in solidification morphology in TRIP and DP steel welds, the tensile strain distribution is also different. Due to a steep angle of impingement of columnar grains at the centre in TRIP steel, a continuous liquid film is formed at the centre [1]. As a result, transverse strain is mostly concentrated at the centreline as shown in Fig. 8 (a). In DP steel, multiple columnar grains bend towards the centreline and strain is partitioned among several grain boundary liquid films (Fig. 8(b)).

Fig. 8(c–d) shows a schematic of the transverse strain distribution across the mushy region in both the steels. Solidification starts at the fusion boundary and the solid-liquid interface grows towards the weld centre. At the last stages of solidification, the material close to the fusion boundary is strong (high yield strength) compared to the weld centre. Thus, the transverse strain in the solid increases as one moves from the fusion boundary to the weld centre. In the presence of grain boundary liquid films, the transverse strain in the liquid films also increases. Due to the morphology of the grain boundaries in DP steel, the transverse strain is partitioned among several liquid films. In addition, a high coherency temperature in DP steel reduces the time during which the grain boundary liquid films persist. The overall mushy region is therefore relatively strong in DP steel.

In the case of TRIP steel, the coherency temperature is low, *i.e.* the grain boundary liquid films persist for a longer time. The overall mushy region is therefore weak. In presence of a concentrated

transverse strain at the weld centre, there is a higher likelihood of solidification cracking. In other words, the threshold strain for solidification cracking in TRIP steel is lower than in DP steel. Note that the grain size also has an influence on solidification cracking. With a reduction in grain size, the grain boundary area increases and the degree of segregation of harmful elements (*e.g.* P) decreases. As a consequence, the resistance to solidification cracking increases [1].

3.3. Weld pool shape difference in TRIP and DP steel

It is well known that the weld pool shape (teardrop or elliptical) depends on the heat source travel speed. With increasing speed, the weld pool shape changes from circular, to elliptical and finally to a teardrop shape [56]. For the same welding parameters, the weld pool shape was observed to be different for the TRIP and DP steels, which must be related to the thermophysical properties, that in turn depend on the chemical composition. The thermal gradient is a minimum at the tail of the weld pool. If the latent heat of fusion generated upon solidification exceeds the heat dissipation at the centre, the weld pool elongates and eventually becomes teardrop shaped [53].

Fig. 9(a–b) shows the calculated weld pool shape for both TRIP and DP steel welds for similar welding conditions. The difference in the tail of the weld pool shape can be attributed to the thermal diffusivity. Due to higher thermal diffusivity of the DP steel (Fig. 10), the latent heat released upon solidification is dissipated faster than for the TRIP steel. Therefore, accurate determination of thermophysical properties is essential to correctly predict the weld pool shape. For both the steels, the geometries of the experimentally obtained weld cross sections were compared with the thermal model and found to be in reasonably good agreement. This information is available in the Supplementary data.

Fig. 9(c–d) shows the calculated liquidus and solidus isotherms in both the steels. The solidus temperature of TRIP (1593 K) and DP (1716 K) steel was calculated based on Scheil-Gulliver model. In the Scheil-Guliver model, all the alloying elements (Fe, C, Mn, Si,
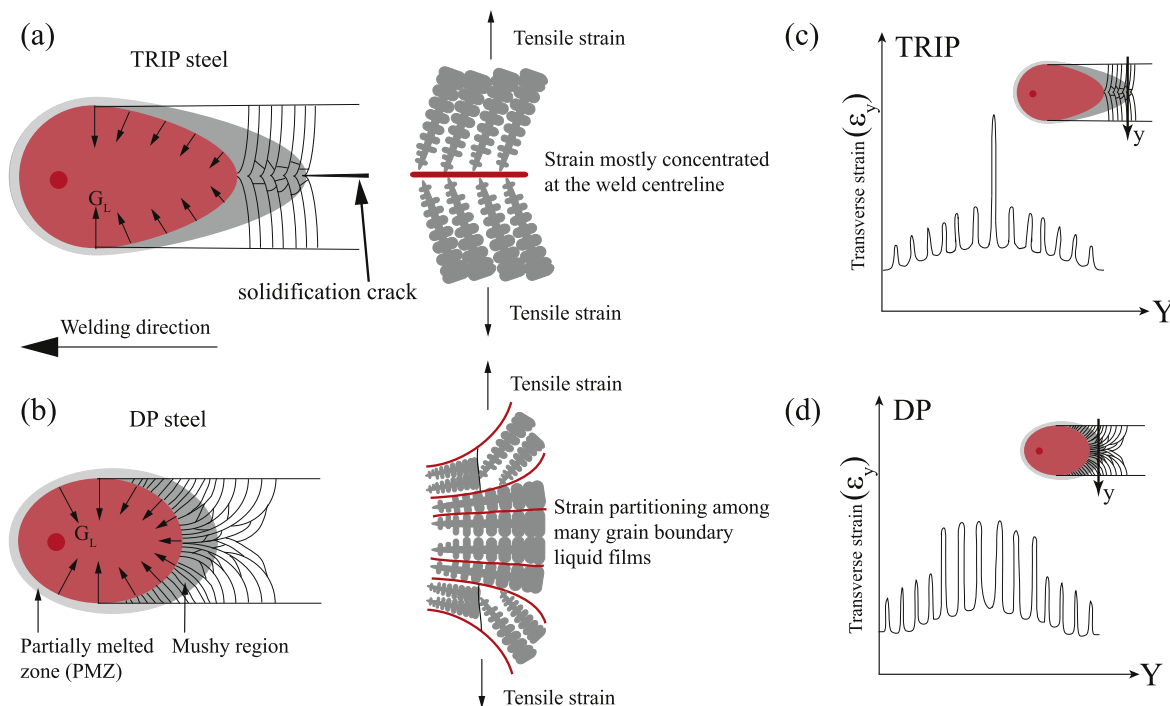

Fig. 8. (a–b) The effect of solidification morphology (weld pool shape) on strain partitioning. (a) Teardrop weld pool shape leads to higher cracking sensitivity (b) in DP steel, strain is partitioned among several grain boundaries leading to higher cracking resistance. (c–d) Schematic showing the transverse strain distribution along the mushy region in the transverse direction. (c) in TRIP steel, the strain is concentrated at the liquid film present at the weld centre, (d) the transverse strain in the case of DP steel is partitioned among several liquid films present at the grain boundaries.
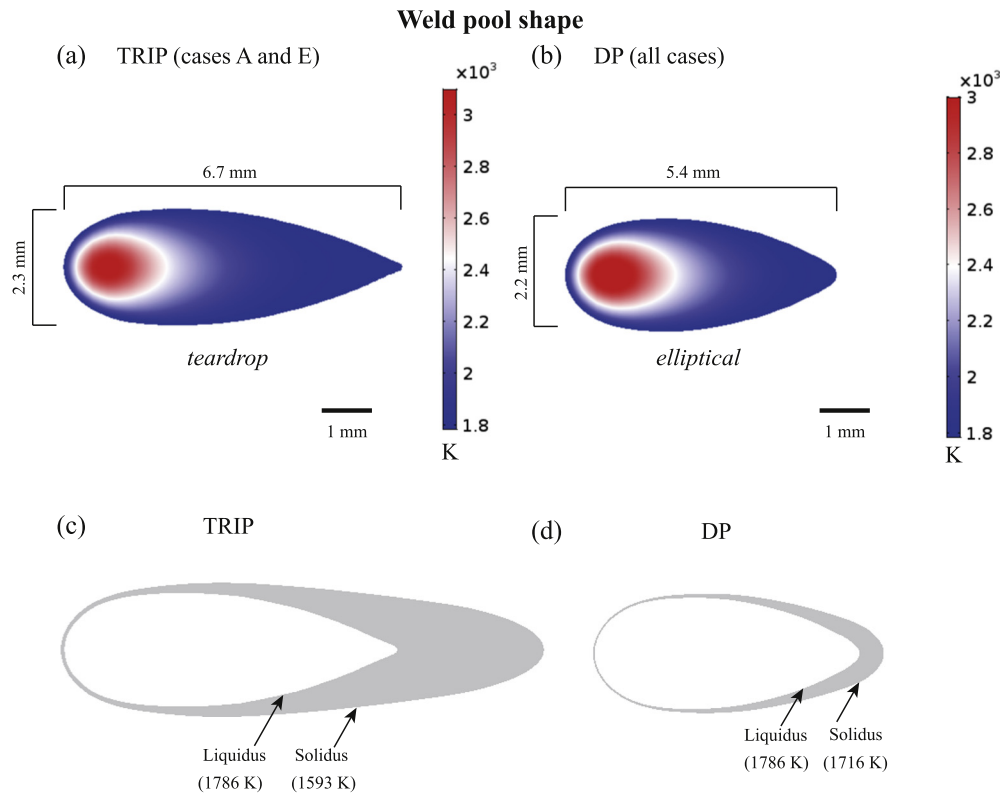
Weld pool shape

Fig. 9. (a–b) Weld pool shape calculated by finite element thermal model. (a) Cases A and E in TRIP steel and (b) DP steel. (c–d) Liquidus and solidus isotherms calculated by finite element thermal model. Solidus temperature is based on Scheil-Gulliver solidification model.

Al, Cr and P) were considered. Due to an extended solidification temperature range in the TRIP steel, the size of the mushy region is considerably large when compared to the DP steel.

The recent models on solidification cracking [22, 57, 20] tacitly assume that the weld pool shape does not change for a given alloy series (*e.g.* Al-Cu alloys), under the same welding parameters. As the evidence here shows, the assumption could be wrong even in alloys which are not vastly different in their compositions. Weld pool shape directly governs the solidification morphology (interface growth rate, PDAS, SDAS) and thus the strength of the mushy region.
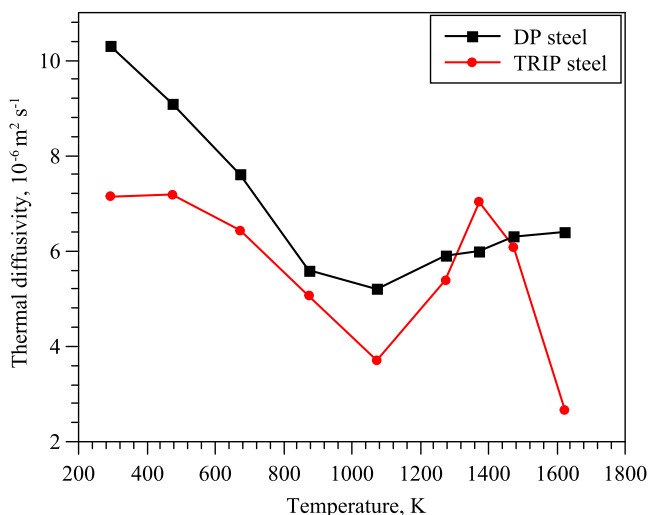

Fig. 10. Thermal diffusivity as a function of temperature of DP and TRIP steel.

3.4. Effect of weld pool shape on solidification cracking in TRIP steel

From the previous discussion, it is apparent that TRIP steel is susceptible to solidification cracking. Cracking was observed in all cases with the exception of case D (Table 2). A numerical and experimental study was carried out to show the effect of weld pool shape on solidification cracking behaviour.

The weld pool shape of the TRIP steel was calculated for cases B to D, using the FE-thermal model. The heat input was kept constant, *i.e.* 110 J mm^{-1} for all the cases. As the travel speed decreases from 10 mm s^{-1} to 7 mm s^{-1}, the weld pool shape changes from teardrop to elliptical (Fig. 11). Also, the size of the mushy zone decreases.

Welding experiments were conducted for these conditions. Complete fracture was observed in cases B and C. Solidification cracking was not observed in any of the experiments for case D. In the latter case, an optical micrograph of the top surface (Fig. 12) shows bending of grains towards the weld centre indicating that the weld pool shape was elliptical. It can be inferred that the threshold strain required for cracking increases in case D. The arguments given to explain the resistance towards solidification cracking in DP steel also hold true in case D for TRIP steel.

3.5. Dominant aspects of solidification cracking

This manuscript has focussed on describing the interplay between the fundamental factors which affect the susceptibility to solidification cracking. The models proposed by Rappaz et al. [20] and Kou [22] are based on a threshold strain rate beyond which cracking can occur. Nonetheless, a combination of minimum local strain and local strain rate is essential for the initiation of a solidification crack. Fig. 13(a) shows the schematic of a typical hot ductility curve [2]. From this
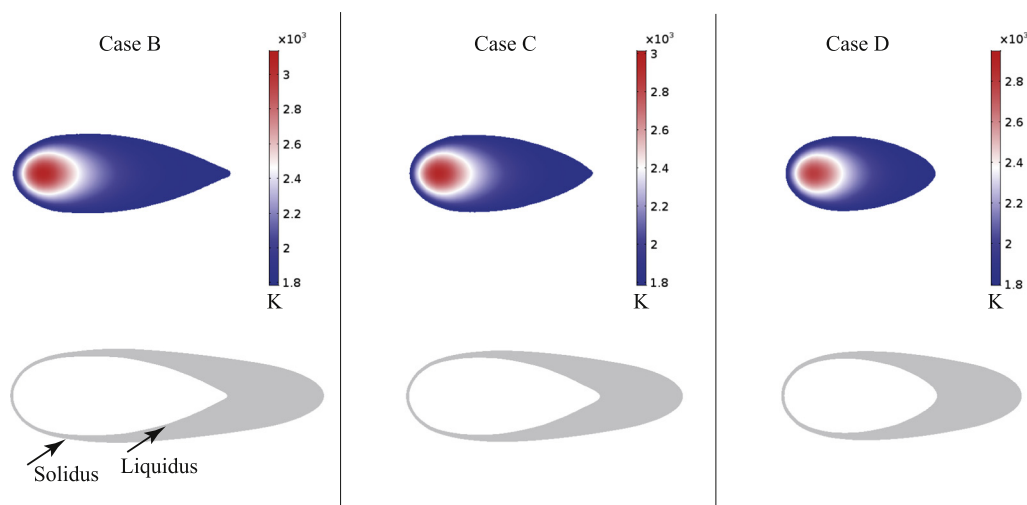
Fig. 11. Weld pool shape in cases B, C and D calculated by the finite element thermal model for TRIP steel. Liquidus and solidus isotherms are also shown. Solidus temperature is based on Scheil-Gulliver solidification model.

curve, the strain imposed on the mushy region is related to the strain rate by:

$$\frac{d\varepsilon}{dT} = \frac{d\varepsilon}{dt}\frac{dt}{dT}. \tag{7}$$

The effect of the strain rate on the minimum strain required for crack initiation depends on the nature of the ductility curve of the material in question. For example, consider the ductility curve for materials A and B shown in Fig. 13(a) and (b), respectively. For material A, when a high strain rate is imposed on the mushy region (line A in Fig. 13(a)), the strain required for crack initiation decreases (ε_A). Conversely, when a lower strain rate is imposed on the mushy region (line B in Fig. 13(a)), the required strain for crack initiation increases ($\varepsilon_B > \varepsilon_A$). However, this effect is reversed if the ductility curve of a material is different, an example of which is shown in the ductility curve of material B (Fig. 13(b)). Matsuda et al. [58] reported ductility curves for plain carbon steels, in which the curves for 0.08 wt % C and 0.16 wt % C have similar shapes to the schematic curves for materials A and B, respectively.

Whether a material in the mushy state is able to withstand the imposed strain (rate) or not, depends on several aspects (Fig. 1). Under a given set of welding conditions, the ductility curve of a material is unique, *i.e.* the ductility curve of a material changes as the welding conditions are altered. Welding conditions lead to a change in the dendrite size, shape, orientation and growth rate which affects the hot ductility curve. Take for example, the ductility curves of material A in Fig. 13(c) and (d). By changing the welding conditions, the ductility curve of the material A can shift upward as shown in

TRIP weld surface, case D
(bending of grains near weld centreline)

500 μm

Fig. 12. Macrograph of the weld surface of TRIP steel for case D.

Fig. 13(d). This could, for example, be achieved by having an elliptically shaped weld pool which can increase the strength of the mushy region and for which, the minimum strain required for crack initiation increases. In the ductility curves shown in Fig. 13(c) and (d), $\varepsilon_E > \varepsilon_A$ and cracking cannot occur if the strain imposed follows line F in Fig. 13(d). This hypothesis is supported by the experimental observations on the TRIP steel welds (cases B and D in Fig. 11).

4. Conclusions

Solidification cracking occurs due to the strain induced in the mushy region by the welding process in combination with the metallurgical features prevailing during weld metal solidification. In general, TRIP steel was found to be susceptible towards solidification cracking. In DP steels, solidification cracking was not observed for the welding conditions studied. Following conclusions are drawn from this study,

1. TRIP steel with high P showed considerable segregation of phosphorus at the grain boundaries. Therefore, the solidification temperature range is extended considerably which is confirmed by the presence of inclusions. In DP steel with low P, segregation was found to be limited and the solidification temperature range does not increase significantly.
2. Under similar welding conditions, the weld pool in TRIP steel has a teardrop shape while in DP steel the shape is elliptical. The morphology of the weld metal is accordingly different. In DP steel, the solidifying grains bend continuously whereas in TRIP steel the grains grow mostly in one direction. Therefore, the solid-liquid interface grows at a slower rate in TRIP steel, which in combination with phosphorus segregation leads to the presence of liquid films for longer duration. This increases the solidification cracking susceptibility in TRIP steel.
3. Due to the presence of continuous grain boundary liquid films at the weld centre, the transverse strain in TRIP steel (except case D) should mostly be concentrated at the weld centreline. In DP steel, the transverse strain should be partitioned among several grain boundary liquid films. The strain does not exceed the threshold strain required for rupturing of the liquid films.
4. For accurate prediction of the weld pool tail, determination of the high temperature thermophysical properties is essential. Small deviations in the thermal diffusivity can lead to a change in the weld pool shape.
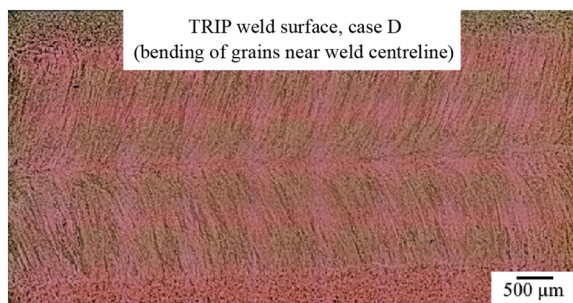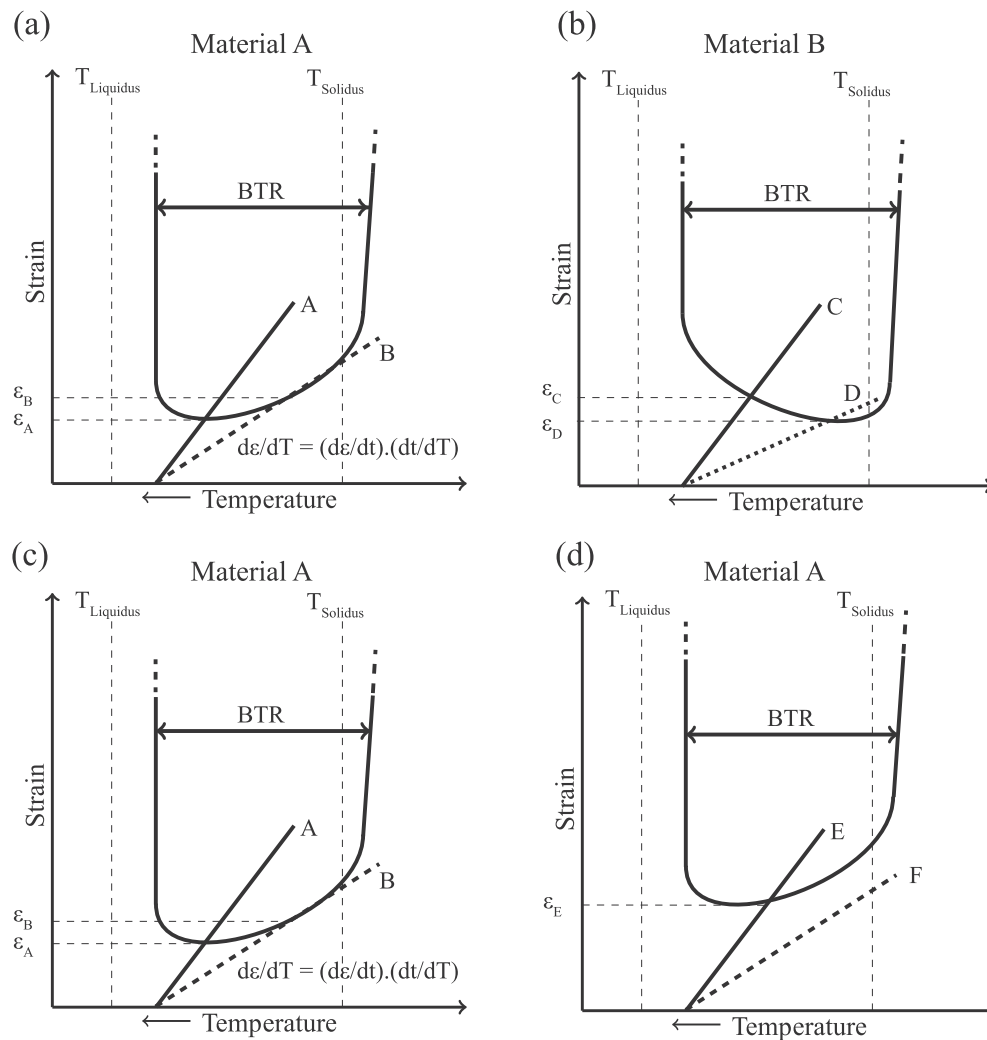
Fig. 13. Schematic of the ductility curve for materials A and B. (a) Ductility curve of material A, (b) ductility curve of material B, (c) ductility curve of material A under a given welding conditions and (d) ductility curve of material A when different welding conditions exist. The ductility curves in (a) and (c) are identical; (c) and (d) are placed side by side for better visualisation of the difference. BTR stands for brittle temperature range [2].

5. A sufficiently accurate thermal model can be used to determine the conditions that result in a preferable elliptical shape. This was confirmed by experiments, in which solidification cracking was also not observed.

CRediT authorship contribution statement

G. Agarwal: Conceptualization, Methodology, Validation, Formal analysis, Investigation, Writing - original draft, Visualization. **A. Kumar:** Data curation, Methodology, Writing - review & editing. **I.M. Richardson:** Writing - review & editing, Supervision, Project administration, Funding acquisition. **M.J.M. Hermans:** Resources, Writing - review & editing, Supervision, Project administration, Funding acquisition.

Acknowledgments

Appendix A. Supplementary data

Supplementary data to this article can be found online at https://doi.org/10.1016/j.matdes.2019.108104.

Data availability statement

The data supporting the findings of this study will be made available on request.

References

[1] S. Kou, Welding Metallurgy, second ed., John Wiley & Sons, Inc. 2003.
[2] J. Lippold, Welding Metallurgy and Weldability, first ed., John Wiley & Sons. 2014.
[3] M.C. Flemings, Solidification Processing, Mc Graw Hill, New York, 1974.

[4] M. Rappaz, J. Dantzig, Solidification, first ed., EFPL Press. 2009.
[5] C. Fink, An investigation on ductility-dip cracking in the base metal heat-affected zone of wrought nickel base alloys—part i: metallurgical effects and cracking mechanism, Weld. World 60 (5) (2016) 939–950. https://doi.org/10.1007/s40194-016-0370-4.
[6] T. Kannengießer, T. Böllinghaus, Hot cracking tests — an overview of present technologies and applications, Weld. World 58 (3) (2014) 397–421. https://doi.org/10.1007/s40194-014-0126-y.
[7] N. Wang, S. Mokadem, M. Rappaz, W. Kurz, Solidification cracking of superalloy single-and bi-crystals, Acta Mater. 52 (11) (2004) 3173–3182. https://doi.org/10.1016/j.actamat.2004.03.047.
[8] M.E. Glicksman, Principles of Solidification: An Introduction to Modern Casting and Crystal Growth Concepts, Springer New York, New York NY, 2011.
[9] Z. Yang, A. Bandivadekar, Light-duty Vehicle Greenhouse Gas and Fuel Economy Standards, Tech. Rep., The International Council on Clean Transportation. 2017.
[10] S. Keeler, M. Kimchi, P.J. Mconey, Advanced High-strength Steels Application Guidelines, Tech. Rep. 6.0, World Auto Steel. 2017.
[11] T. Hilditch, T. de Souza, P. Hodgson, 2 — Properties and Automotive Applications of Advanced High-Strength Steels (Ahss), in: M. Shome (Ed.), Welding and Joining of Advanced High Strength Steels (AHSS), Woodhead Publishing. 2015, pp. 9–28. https://doi.org/10.1016/B978-0-85709-436-0.00002-3.
[12] C. Lesch, N. Kwiaton, F.B. Klose, Advanced high strength steels (ahss) for automotive applications & tailored properties by smart microstructural adjustments, Steel Res. Int 88 (10) (2017) 1700210. https://doi.org/10.1002/srin.201700210.
[13] J.K. Larsson, Avoidance of crack inducement when laser welding hot-formed car body components — a variable analysis, Phys. Procedia 5 (2010) 115–124. laser Assisted Net Shape Engineering 6, Proceedings of the LANE 2010, Part 2. https://doi.org/10.1016/j.phpro.2010.08.036.
[14] C.E. Cross, On the Origin of Weld Solidification Cracking, in: T. Böllinghaus (Ed.), Hot Cracking Phenomena in Welds, Springer Berlin Heidelberg. 2005, pp. 3–18. https://doi.org/10.1007/3-540-27460-X_1.
[15] W.S. Pellini, Strain theory of hot-tearing, Foundry 80 (1952) 124–133.
[16] N.N. Prokhorov, The problem of the strength of metals while solidifying during welding, Svar. Proizvod. 6 (1956) 5–11.
[17] I. Medovar, On the nature of weld hot cracking, Avtom. Svarka 7 (1954) 12–28.
[18] D.G. Eskin, L. Katgerman, A quest for a new hot tearing criterion, Metall. Mater. Trans. A 38 (7) (2007) 1511–1519. https://doi.org/10.1007/s11661-007-9169-7.
[19] U. Feurer, Influence of Alloy Composition and Solidification Conditions on Dendrite Arm Spacing, Feeding, and Hot Tear Properties of Aluminum Alloys, Proceedings of the International Symposium on Engineering Alloys, 1977, pp. 131–145. Delft.
[20] M. Rappaz, J.M. Drezet, M. Gremaud, A new hot-tearing criterion, Metall. Mater. Trans. A 30 (2) (1999) 449–455. https://doi.org/10.1007/s11661-999-0334-z.
[21] N. Coniglio, C. Cross, Mechanisms for solidification crack initiation and growth in aluminum welding, Metall. Mater. Trans. A 40 (11) (2009) 2718–2728. https://doi.org/10.1007/s11661-009-9964-x.
[22] S. Kou, A criterion for cracking during solidification, Acta Mater. 88 (2015) 366–374. https://doi.org/10.1016/j.actamat.2015.01.034.
[23] G. Agarwal, Study of Solidification Cracking during Laser Welding in Advanced High Strength Steels, ph.D. thesis. TU Delft. 2019. https://doi.org/10.4233/uuid:dd0e5ab0-1427-4ecc-a8d8-4e8f35050fca.
[24] S. VDEh, SEP 1220-3: Testing and Documentation Guideline for the Joinability of Thin Sheet of Steel — Part 3: Laser Beam Welding, 2011.
[25] G. Agarwal, H. Gao, M. Amirthalingam, M. Hermans, Study of solidification cracking susceptibility during laser welding in an advanced high strength automotive steel, Metals 8 (9)10.3390/met8090673.
[26] S.A. David, T. DebRoy, Current issues and problems in welding science, Science 257 (5069) (1992) 497–502. https://doi.org/10.1126/science.257.5069.497.
[27] J.W. Elmer, S.M. Allen, T.W. Eagar, Microstructural development during solidification of stainless steel alloys, Metall. Trans. A 20 (10) (1989) 2117–2131. https://doi.org/10.1007/BF02650298.
[28] C. Cayron, B. Artaud, L. Briottet, Reconstruction of parent grains from ebsd data, Mater. Charact 57 (4) (2006) 386–401. https://doi.org/10.1016/j.matchar.2006.03.008.
[29] C. Cayron, ARPGE: a computer program to automatically reconstruct the parent grains from electron backscatter diffraction data, J. Appl. Cryst. 40 (6) (2007) 1183–1188. https://doi.org/10.1107/S0021889807048777.
[30] A. Kumar, G. Agarwal, R. Petrov, S. Goto, J. Sietsma, M. Herbig, Microstructural evolution of white and brown etching layers in pearlitic rail steels, Acta Mater. 171 (2019) 48–64. https://doi.org/10.1016/j.actamat.2019.04.012.
[31] N. Shanmugam, G. Buvanashekaran, K. Sankaranarayanasamy, S.R. Kumar, A transient finite element simulation of the temperature and bead profiles of t-joint laser welds, Mater. Des 31 (9) (2010) 4528–4542. https://doi.org/10.1016/j.matdes.2010.03.057.
[32] J. Ma, F. Kong, R. Kovacevic, Finite-element thermal analysis of laser welding of galvanized high-strength steel in a zero-gap lap joint configuration and its experimental verification, Mater. Des 36 (2012) 348–358. https://doi.org/10.1016/j.matdes.2011.11.027.

[33] M.Z. ul abdein, D. Nélias, J.-F. Jullien, D. Deloison, Experimental investigation and finite element simulation of laser beam welding induced residual stresses and distortions in thin sheets of aa 6056-t4, Mater. Sci. Eng. A 527 (12) (2010) 3025–3039. https://doi.org/10.1016/j.msea.2010.01.054.
[34] H. Gao, Residual Stress Development Due to High-Frequency Post Weld Impact Treatments for High-Strength Steels, ph.D. thesis. TU Delft. 2014. https://doi.org/10.4233/uuid:2029863f-4967-4796-ba4f-199dca8c7212.
[35] E. van der Aa, Local Cooling during Welding: Prediction and Control of Residual Stresses and Buckling Distortion,ph.D. thesis. TU Delft. 2007.
[36] E.A.A. Ahmed, Laser Welding of Advanced High Strength Steels,ph.D. thesis. RWTH Aachen. 2011.
[37] Standard, Advanced Technical Ceramics — Monolithic Ceramics Thermophysical Properties — Part 2: Determination of Thermal Diffusity by the Laser Flash (or heat pulse) Method; German Version en 821-2, 1997.
[38] Standard, Advanced Technical Ceramics — Monolithic Ceramics — Thermophysical Properties — Part 3: Determination of Specific Heat Capacity; German Version en 821-3, 2005.
[39] R. Rai, G.G. Roy, T. DebRoy, A computationally efficient model of convective heat transfer and solidification characteristics during keyhole mode laser welding, J. Appl. Phys 101 (5) (2007) 054909. https://doi.org/10.1063/1.2537587.
[40] R. Rai, J.W. Elmer, T.A. Palmer, T. DebRoy, Heat transfer and fluid flow during keyhole mode laser welding of tantalum, Ti-6Al-4V, 304l stainless steel and vanadium, J. Phys. D. Appl. Phys 40 (18) (2007) 5753–5766. https://doi.org/10.1088/0022-3727/40/18/037.
[41] Y. Pan, Laser Welding of Zinc Coated Steel without Pre-Set Gap,ph.D. thesis. TU Delft. 2011.
[42] T. Soysal, S. Kou, A simple test for assessing solidification cracking susceptibility and checking validity of susceptibility prediction, Acta Mater. 143 (2018) 181–197. https://doi.org/10.1016/j.actamat.2017.09.065.
[43] J. Zhang, R. Singer, Hot tearing of nickel-based superalloys during directional solidification, Acta Mater. 50 (7) (2002) 1869–1879. https://doi.org/10.1016/S1359-6454(02)00042-3.
[44] C.E. Cross, T. Boellinghaus, The effect of restraint on weld solidification cracking in aluminium, Weld. World 50 (11) (2006) 51–54. https://doi.org/10.1007/BF03263461.
[45] G. Goodwin, Development of a new hot-cracking test — the sigmajig, Weld. J. (1987) 33–38. (Miami); (United States) 66:2.
[46] H. Gao, G. Agarwal, M. Amirthalingam, M.J.M. Hermans, I.M. Richardson, Investigation on hot cracking during laser welding by means of experimental and numerical methods, Weld. World 62 (1) (2018) 71–78. https://doi.org/10.1007/s40194-017-0524-z.
[47] G. Agarwal, A. Kumar, H. Gao, M. Amirthalingam, S.C. Moon, R.J. Dippenaar, I.M. Richardson, M.J.M. Hermans, Study of solidification cracking in a transformation-induced plasticity-aided steel, Metall. Mater. Trans. A 49 (4) (2018) 1015–1020. https://doi.org/10.1007/s11661-018-4505-7.
[48] F. Matsuda, S. Katayama, Y. Arata, Solidification crack susceptibility in weld metals of fully austenitic stainless steels (report v): solidification crack susceptibility and amount of phosphide and sulphide in sus 310s weld metals, Trans JWRI 10 (2) (1981) 201–212.
[49] M. Quintana, J. McLane, S. Babu, S. David, Inclusion formation in self-shielded flux cored arc welds, Weld. J. 80 (2001) 98s–105s.
[50] V. Shankar, T.P.S. Gill, S.L. Mannan, S. Sundaresan, Solidification cracking in austenitic stainless steel welds, Sadhana 28 (3) (2003) 359–382. https://doi.org/10.1007/BF02706438.
[51] W.F. Savage, Solidification, segregation weld imperfections, Weld. World 18 (5) (1980) 89–114.
[52] M. Rappaz, S.A. David, J.M. Vitek, L.A. Boatner, Development of microstructures in Fe-15Ni-15Cr single crystal electron beam welds, Metall. Trans. A 20 (6) (1989) 1125–1138. https://doi.org/10.1007/BF02650147.
[53] S.A. David, J.M. Vitek, Correlation between solidification parameters and weld microstructures, Int. Mater. Rev 34 (1) (1989) 213–245. https://doi.org/10.1179/imr.1989.34.1.213.
[54] H. Wei, J. Elmer, T. DebRoy, Origin of grain orientation during solidification of an aluminum alloy, Acta Mater. 115 (2016) 123–131. https://doi.org/10.1016/j.actamat.2016.05.057.
[55] G. Agarwal, M. Amirthalingam, S.C. Moon, R.J. Dippenaar, I.M. Richardson, M.J.M. Hermans, Experimental evidence of liquid feeding during solidification of a steel, Scr. Mater. 146 (2018) 105–109. https://doi.org/10.1016/j.scriptamat.2017.11.003.
[56] R. Trivedi, S.A. David, M.A. Eshelman, J.M. Vitek, S.S. Babu, T. Hong, T. DebRoy, In situ observations of weld pool solidification using transparent metal-analog systems, J. Appl. Phys 93 (8) (2003) 4885–4895. https://doi.org/10.1063/1.1559934.
[57] S. Kou, A simple index for predicting the susceptibility to solidification cracking, Weld. J. 94 (12) (2015) 374s–388s.
[58] F. Matsuda, H. Nakagawa, H. Kohmoto, Y. Honda, Y. Matsubara, Quantitative evaluation of solidification brittleness of weld metal during solidification by in-situ observation and measurement (report ii), Trans JWRI 12 (1983) 73–80.